arXiv:2605.09724v2 [cs.LG] 9 Oct 2026

Model Capacity Determines Grokking through Competing Memorisation and Generalisation Speeds

Yiding 'Vincent' Song
Harvard College
Cambridge, MA 02138
yidingsong@college.harvard.edu

Hanming Ye
Harvard College
Cambridge, MA 02138
hanmingye@college.harvard.edu

Abstract

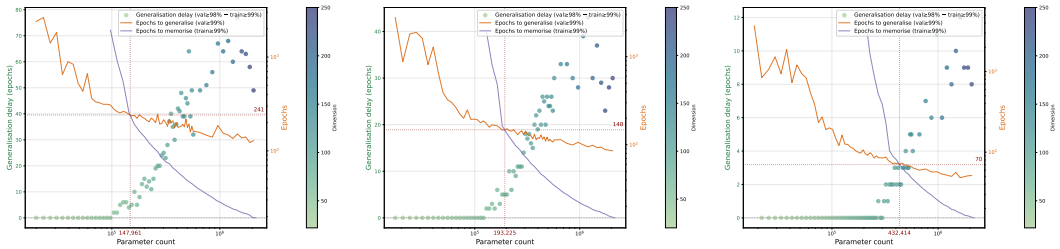
Existing accounts of grokking explain the phenomena in terms of mechanistic frameworks such as circuit efficiency or lazy-to-rich transitions. However, despite a known dependence between grokking and model size, how model capacity shapes grokking remains an open question. We give an information-theoretic account of this relationship on the task of modular arithmetic, showing that grokking does not immediately occur when a model becomes large enough to memorise the training set, but rather emerges as the outcome of a competition between two measurable timescales: a memorisation speed $T_{\text{mem}}(P)$ and a generalisation speed $T_{\text{gen}}(P)$, both of which are functions of model parameter count P. Adapting the information capacity framework of Morris et al. [2025], we estimate $T_{\text{mem}}(P)$ on random-label data of equivalent complexity and $T_{\text{gen}}(P)$ on the modular task itself, and show that grokking emerges close to the parameter scale where these timescales intersect. The framework also suggests an empirical model for predicting memorisation speed given model capacity and dataset complexity, recovering the previously reported empirical observation that larger models memorise faster. Overall, we motivate the formalisation of different learning timescales as important abstractions to study when explaining how model capacity shapes grokking on algorithmic tasks.

1 Introduction

The grokking phenomenon [Power et al., 2022] on modular arithmetic, whereby training accuracy saturates long before test accuracy, has become a canonical testbed for the dynamics of memorisation and generalisation in overparameterised networks. Existing accounts identify mechanisms that select the eventual generalising solution: implicit-bias and lazy-to-rich dynamical transitions [Lyu et al., 2024, Kumar et al., 2024], circuit-efficiency arguments under weight decay [Varma et al., 2023, Huang et al., 2024], selective norm growth that sparsifies the network [Merrill et al., 2023], kernel-regime impossibility for modular addition [Mohamadi et al., 2024], and mechanistic reverse engineering of grokked Transformers [Nanda et al., 2023]. These accounts pinpoint why a generalising solution is preferred at convergence.

However, the existing body of work does not explain fully how grokking depends on model size. Empirically, several papers have observed that very small models on modular arithmetic do not exhibit grokking at all, generalising immediately instead [Liu et al., 2022a, Huang et al., 2024]; only past some larger scale does the characteristic delay appear. A natural prediction follows from the bits-per-parameter capacity framework of Morris et al. [2025]: grokking should begin once model capacity exceeds the dataset size, since that is where the memorising solution first becomes representable. Empirically, however, models with parameter counts well above this threshold continue to generalise immediately; the onset of grokking sits at a parameter count strictly larger than the capacity threshold. This leaves open the question of what controls the parameter scale at which grokking begins, if not the capacity threshold itself.

Preprint.



(a) $p = 97$ (b) $p = 113$ (c) $p = 139$

Figure 1: Generalisation delay (scatter, left axis: number of epochs between model reaching high training accuracy and high validation accuracy; colour encodes model dimension d) and learning speeds (orange: epochs to generalise; purple: epochs to memorise random dataset of same complexity) versus model parameter count for three primes. The dashed crosshair marks the predicted grokking point $\widehat{P}_{\text{cross}}(p)$, given by the intersection of the generalisation (orange) and memorisation (purple) curves; this coincides closely with the onset of non-zero generalisation delay (i.e. 'grokking'). For small models, generalisation is faster than memorisation and the model generalises immediately (zero delay, no grokking). As parameter count P increases, memorisation speed approaches generalisation speed; once the two cross, generalisation delays become non-zero and grokking begins.

We argue that the missing ingredient is a quantitative treatment of *learning timescales*. Building on the bits-per-parameter capacity methodology of Morris et al. [2025], we define two measurable speeds for a Transformer of size P: a **memorisation speed** $T_{\text{mem}}(P)$, the number of epochs to fit a random-label dataset of equivalent information content; and a **generalisation speed** $T_{\text{gen}}(P)$, the number of epochs to reach high validation accuracy on the modular task. We focus on modular division over prime fields and a family of small decoder-only Transformers. Our central finding is that the onset of grokking coincides closely with the parameter count at which these two timescales intersect, a count that is strictly larger than the capacity threshold P_{mem} at which memorisation first becomes representable. A capacity sufficient to represent a memorising solution is not sufficient to make memorisation the path that gradient descent takes; what matters is whether memorisation is faster than generalisation.

Concretely, we observe three regimes as we scale model parameter count P (Fig. 1): an **under-capacity** regime (model capacity well below the dataset complexity) in which neither solution is represented and both train and test accuracy are low; an **immediate-generalisation** regime in which model capacity is comparable to or exceeds the dataset complexity but $T_{\text{gen}}(P) < T_{\text{mem}}(P)$, so gradient descent reaches the algorithmic solution before any memorisation completes and there is no generalisation delay; and a **grokking** regime, beyond the speed intersection, in which $T_{\text{mem}}(P) \lesssim T_{\text{gen}}(P)$ and the model first memorises and only later generalises.

Our main contributions in this paper are:[1]

1. **A mechanistic account of how capacity controls grokking, via competing memorisation and generalisation speeds.** Adapting the bits-per-parameter framework of Morris et al. [2025], we formalise measurements of $T_{\text{mem}}(P)$ and $T_{\text{gen}}(P)$ for small Transformers and show that the parameter count at which they intersect closely tracks the empirical onset of grokking across primes and dataset sizes.
2. **Two prior observations recovered as separate consequences of the framework.** The empirical observation that small models on modular arithmetic do not grok [Liu et al., 2022a, Huang et al., 2024] follows from our framework because at small P, $T_{\text{gen}}(P) < T_{\text{mem}}(P)$, so the generalising solution is reached first. The observation that larger language models memorise faster [Tirumala et al., 2022] is recovered, in our setting, by the empirical regularity that $T_{\text{mem}}(P, n)$ depends primarily on the capacity fraction $f = K/(C_{\text{model}}P)$, where K is dataset size and C_{model} is model capacity, with $T_{\text{mem}} \propto e^{af}$ for $f \in [0, 0.25]$ (Fig. 3b). Both empirical observations follow from distinct components of our framework.

[1]The code needed to reproduce and visualise the results in this paper is available at `https://github.com/PerceptronV/grokking-capacity`.

2 Background and Related Work

Grokking and algorithmic generalisation. Grokking, or delayed generalisation after rapid training-set overfitting, was introduced by Power et al. [2022] in small Transformers trained on algorithmic tasks such as modular addition. Modular arithmetic has since served as a controlled testbed for separating memorisation from algorithmic solutions and for probing the dynamics that mediate between them, with mechanistic reverse engineering of the grokked Fourier algorithm [Nanda et al., 2023] and extensions to richer modular families and reasoning-like compositions [Furuta et al., 2024, Wang et al., 2024, He et al.]. Grokking-like transitions have also been reported beyond algorithmic data, suggesting that delayed generalisation is not specific to modular arithmetic but reflects more general properties of overparameterised optimisation [Liu et al., 2022b, Humayun et al., 2024].

Mechanistic accounts: why a generalising solution is preferred. A body of work explains grokking by identifying mechanisms that select the generalising solution. Varma et al. [2023] attribute the late switch to circuit efficiency: weight decay favours a norm-efficient generalising circuit over a memorising lookup, and Huang et al. [2024] extend this competition picture to a 2D phase diagram over model size and dataset size that includes a small-model 'progression' regime of immediate generalisation. Merrill et al. [2023], in a sparse-parity setting, document grokking as the emergence of a sparse subnetwork via selective norm growth in a small set of neurons. Liu et al. [2022a] earlier mapped a four-phase diagram (comprehension, grokking, memorisation, confusion) on modular arithmetic and noted a small-decoder regime that does not grok, anticipating the empirical phenomenon we focus on here. A complementary line frames grokking as a transition out of the lazy/kernel regime: Kumar et al. [2024] show that grokking can be controlled in a two-layer network by the output-scale "laziness" parameter and the alignment between the initial NTK and the task labels, with grokking arising in a Goldilocks regime where feature learning is delayed; Mohamadi et al. [2024] prove that the kernel regime cannot solve modular addition, providing a static representational counterpart to Kumar et al.'s dynamical claim; and Lyu et al. [2024] derive grokking from a dichotomy between early- and late-phase implicit biases. Phase-transition treatments [Rubin et al., 2023] and complexity-based progress measures [Clauw et al., 2024, DeMoss et al., 2025] interpret grokking as an emergent transition in the network's internal organisation. These accounts identify mechanisms that select the generalising solution but say less about the parameter scale at which grokking appears, or about *when* during training each solution is reached. A recent empirical study [Manir and Rupa, 2026] disentangles depth, architecture, activation, and regularisation effects on modular addition, finding that grokking dynamics are dominated by optimisation–regularisation interactions rather than architectural specifics.

Pattern-learning speeds and timescale-based intuitions. The conceptual ancestor of our framing is the view that grokking arises because different patterns are learned at different rates. Davies et al. [2023] argue that grokking and double descent are unified by a spectrum of pattern-learning speeds: gradient descent first fits fast, poorly-generalising components and only later learns slower, more robust ones. Optimiser-side interventions support this picture: Lee et al. [2024] accelerate grokking dramatically by amplifying slow gradient components, and Thilak et al. [2022] identify late-stage "slingshot" dynamics in adaptive optimisers that often coincide with the grokking transition. Epoch-wise double descent in standard supervised learning likewise reinforces that training time, not only model size, is a meaningful axis of generalisation behaviour [Nakkiran et al., 2020]. Our contribution turns this qualitative speed intuition into two quantitative, separately measurable timescales $T_{\text{mem}}(P)$ and $T_{\text{gen}}(P)$, and shows that their crossover is what controls grokking onset on modular arithmetic — addressing the parameter-scale dependence that the mechanistic accounts above leave open.

Memorisation, capacity, and scaling. The methodological lineage we build on is the use of random-label training to characterise memorisation. Zhang et al. [2017] show that modern networks can interpolate pure noise; Arpit et al. [2017] document the dynamics of this memorisation; and Carlini et al. [2023] quantify it in language models. Most directly, Morris et al. [2025] operationalise memorisation in bits and estimate a bits-per-parameter capacity C_{model} by training to saturation on random tokens. They argue that grokking begins when capacity is saturated. We adopt their measurement framework but use it to characterise learning timescales rather than the static memorisation threshold: grokking onset on modular division falls at the speed crossover, which sits at a parameter count larger than the capacity threshold P_{mem} that Morris et al. [2025] identify. The empirical observation that

larger language models memorise faster [Tirumala et al., 2022] is recovered, in our setting, by the regularity that T_{mem} depends primarily on the capacity fraction $f = K/(C_{\text{model}}P)$.

3 Problem Setting and Notation

3.1 Modular arithmetic datasets

Fix a prime p and an operation $\circ \in \{+, -, \times, /\}$ on $\mathbb{Z}_p$. For modular division we use $a/b \equiv a \cdot b^{-1} \pmod{p}$ with $b \in \{1, \ldots, p-1\}$. Following standard grokking benchmarks, we enumerate all valid pairs (a, b) and build a dataset $\mathcal{D}_p = \{(X_i, y_i)\}_{i=1}^{N_{\text{full}}}$ where each input X_i is a length-4 token sequence encoding the equation $X_i = [a,\ \texttt{op},\ b,\ \texttt{=}]$, and the label $y_i = a \circ b \in \{0, \ldots, p-1\}$. We reserve two special tokens for the operator and equals sign, so the vocabulary size is $V = p + 2$.

For modular division the number of valid pairs is $N_{\text{full}} = p(p-1)$. We randomly select a training subset $\mathcal{D}_p^{\text{train}}$ containing a fraction $\alpha \in (0, 1)$ of these pairs and use the remainder as a held-out test set. Throughout, we focus on $\alpha = 1/2$, so that $N_{\text{train}} = \alpha p(p-1)$ and $N_{\text{test}} = N_{\text{train}}$.

3.2 Dataset complexity and information content

We are interested in the worst-case number of bits needed to memorise the labels y_i given inputs X_i. Assuming random labels, each y_i is uniformly distributed over V possibilities and therefore requires $\log_2 V$ bits to specify. The information content (or *complexity*) of the training data is then

$$K_{\text{mem}}(p, \alpha) = N_{\text{train}} \log_2 V = \alpha p(p-1) \log_2(p+2). \tag{1}$$

We treat modular division as a structured task that admits a much more compact algorithmic description of complexity $K_{\text{alg}}(p)$, although we do not attempt to compute K_{alg} explicitly here.

3.3 Model architecture

All experiments use the same decoder-only Transformer architecture with depth $L_{\text{depth}} = 2$ and a single attention head ($H = 1$). The model receives a sequence of integer token IDs $x \in \{0, \ldots, V-1\}^L$ with $L = 4$ and vocabulary size $V = p + 2$, and outputs logits over the vocabulary for the final position. Each of the two residual blocks contains self-attention with rotary positional embeddings applied to queries and keys, followed by a gated feed-forward network with hidden width $4d$; both sub-blocks are wrapped in RMS normalisation. A final RMSNorm and linear projection from $\mathbb{R}^d$ to $\mathbb{R}^V$ produce the output logits; we vary P by sweeping the embedding width $d \in [10, 1000]$.

3.4 Total memorisation

We briefly summarise the information-theoretic notions of memorisation we use, adapting Morris et al. [2025] to our discrete classification setting. Consider a dataset $D = \{(x_i, y_i)\}_{i=1}^n$ with labels $y_i \in \{1, \ldots, V\}$ and a model $p_\theta(y \mid x)$. We measure log-probabilities in bits, i.e. using $\log_2$.

Definition 3.1 (M_T)**.** The total memorisation of p_θ on D is

$$M_T(\theta; D) = \sum_{i=1}^{n} \left(\log_2 V + \log_2 p_\theta(y_i \mid x_i)\right). \tag{2}$$

Each term is the reduction in code-length (in bits) for example i relative to a uniform baseline that assigns probability $1/V$ to every label. We have $0 \le M_T(\theta; D) \le n \log_2 V$, with the upper bound attained when the model predicts every label with probability 1.

4 Capacity, Learning Speeds, and Grokking

We now formalise our two main quantitative objects: information capacity, measured in bits per parameter, and memorisation/generalisation speeds, measured in the number of training epochs required to reach a saturation threshold.

4.1 Empirical information capacity

Let Θ denote a model architecture (including optimiser and training protocol) with P trainable parameters. We wish to estimate how many bits of label information can be stored in its weights. Following Morris et al. [2025], we train Θ on random-label data. Fix a vocabulary size V and sequence length L. We construct random datasets $D^{\text{rand}} = \{(X_i, Y_i)\}_{i=1}^{n}$, where each input $X_i \in \{0, \dots, V-1\}^L$ is drawn uniformly, and each label $Y_i \in \{0, \dots, V-1\}$ is drawn independently and uniformly, so there is no structure to generalise. We train Θ on D^{rand} until its training accuracy saturates (i.e. equals or exceeds a saturation threshold, set at 99% throughout our experiments) and denote the resulting parameters by $\theta^*(D^{\text{rand}})$. We then compute the total memorisation $M_T(\theta^*(D^{\text{rand}}); D^{\text{rand}})$ via Eq. (2). As we increase n, we obtain a *capacity curve* $M_T(n)$ that initially grows roughly linearly with n (each new datapoint can be memorised) and eventually saturates when the parameters are 'full'. Accordingly , for a given architecture Θ with P parameters we define its capacity as

$$\widehat{\text{Cap}}(\Theta) := \lim_{n \to \infty} M_T(n), \tag{3}$$

approximated in practice by the plateau of the empirical capacity curve. Repeating across a range of model sizes with parameter counts $P_1, \dots, P_K$ yields pairs $(P_k, \widehat{\text{Cap}}_k)$. We then fit a linear model

$$\widehat{\text{Cap}}_k \approx C_{\text{model}} P_k + b, \tag{4}$$

where C_{model} (bits per parameter) is our empirical capacity constant and b is close to zero.

In Section 5.1 we show that for our Transformer family the fit is strongly linear with a small intercept, supporting the view that model capacity is well approximated by a constant number of bits per parameter. Combining C_{model} with the dataset complexity $K_{\text{mem}}(p, \alpha)$ in Eq. (1) yields a rough critical parameter count

$$P_{\text{mem}}(p, \alpha) = \frac{K_{\text{mem}}(p, \alpha)}{C_{\text{model}}}, \tag{5}$$

above which the model could theoretically memorise the entire training set.

4.2 Defining learning speeds

Capacity tells us what is representable, but not what gradient descent actually learns at a given time. To capture dynamics, we treat learning as a competition between two processes: (1) a memorisation process that moves towards a solution approximating the training set; (2) an algorithmic-generalisation process that moves towards a solution implementing modular division. We operationalise these processes using first-passage times under actual training.

Memorisation speed. Fix a model size P, vocabulary size V, and number of training data points n. We train the model on n random-labels using AdamW [Loshchilov and Hutter, 2017] until training accuracy exceeds saturation threshold (we used 99%). We record the total number of epochs taken during that time, denoted $T_{\text{mem}}(P, n)$. For a given prime p, we define the shorthand

$$T_{\text{mem}}(P) := T_{\text{mem}}(P, n_{\text{equiv}}), \quad n_{\text{equiv}} = \frac{K_{\text{mem}}(p, \alpha)}{\log_2 V}, \tag{6}$$

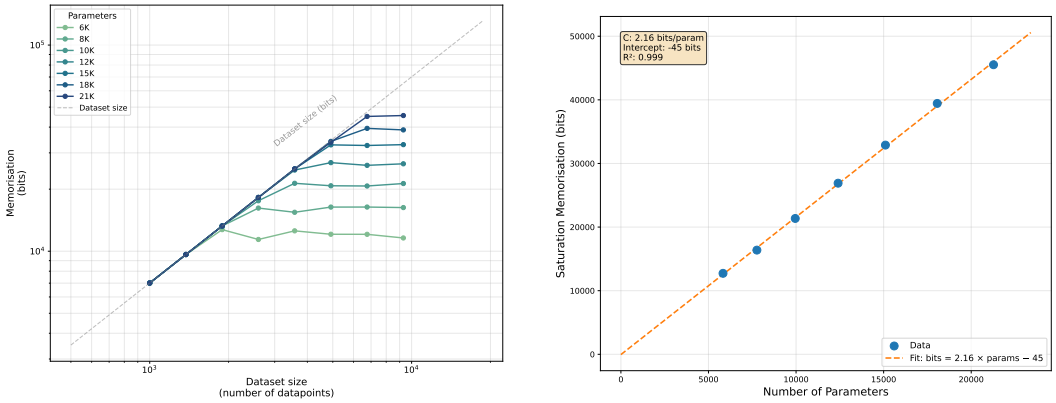
i.e. the expected epochs required to memorise a random dataset with the same total number of bits as the modular-arithmetic dataset with prime p.

In conjunction with memorisation speed, we also define the *capacity fraction*

$$f(P, n_{\text{equiv}}) = \frac{n_{\text{equiv}} \log_2 V}{C_{\text{model}} P} \tag{7}$$

as the ratio of the dataset complexity to the estimated maximum model capacity. We empirically find that $T_{\text{mem}}(P) \propto e^{af}$ for some constant a and $f \in [0, 0.25]$ (Section 5.1).

Generalisation speed. For the modular-division dataset $\mathcal{D}_p^{\text{train}}$, we train the model and monitor validation accuracy on $\mathcal{D}_p^{\text{test}}$. We define the generalisation speed $T_{\text{gen}}(P)$ as the number of epochs taken for validation accuracy to exceed saturation threshold (we used 99%), capturing the time it takes for the model to reach a generalising solution. We computed this quantity across 10 seeds for each model size and took the average.



(a) Total memorisation against dataset complexity.

(b) Saturation memorisation against parameter count.

Figure 2: Random-label capacity experiments following Morris et al. [2025]. Fig. 2a shows total memorisation M_T versus dataset complexity on random-label datasets for several model sizes. The dashed grey line shows the dataset complexity in bits. Fig. 2b plots the highest number of bits a model can memorise versus its parameter count. The slope of the linear fit yields the bits-per-parameter constant C_{model} for our Transformer family.

4.3 Quantifying grokking

Generalisation delay. Separately, we define a generalisation delay

$$\Delta E(P) = \max\left\{0,\, E_{\text{val}}(P) - E_{\text{train}}(P)\right\}, \tag{8}$$

where $E_{\text{train}}(P)$ is the first epoch when training accuracy exceeds 99% and $E_{\text{val}}(P)$ is the first epoch when validation accuracy exceeds 98%. We computed this quantity across 10 seeds for each model size and took the minimum value across seeds, because we are interested in finding the smallest model size for which we consistently observe $\Delta E(P) > 0$. A zero $\Delta E(P)$ corresponds to immediate generalisation. Large positive $\Delta E(P)$ corresponds to grokking: the model fits the training data earlier than it generalises.[2]

Grokking point. We define this as the smallest model size P for which $\Delta E(P') > 0$ for all measured $P' \geq P$ (equivalently: the smallest measured size strictly above the largest non-grokking size); i.e. the smallest model size from which we start to consistently observe grokking.

5 Results

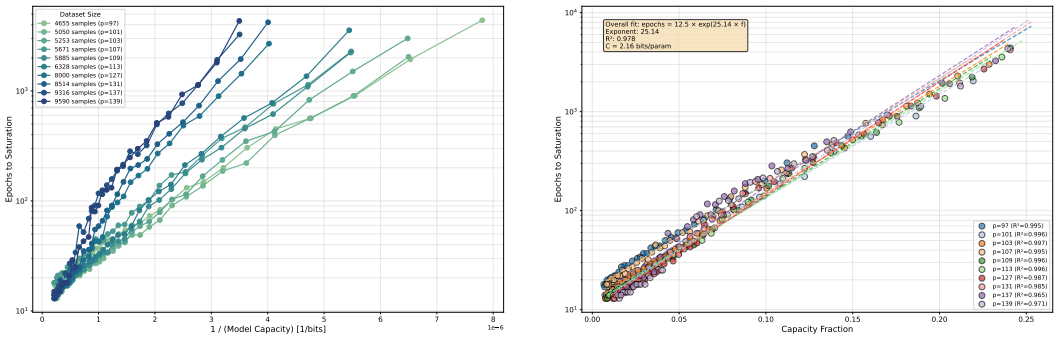
5.1 Model capacity

Fig. 2 shows total memorisation $M_T(n)$ on random data for several model sizes. For small n, the curves grow linearly with slope close to $\log_2 V$, consistent with the model memorising every new label. For larger n they saturate at plateaus $\widehat{\text{Cap}}_k$ that scale linearly with parameter count P_k (Fig. 2, right). Fitting $\widehat{\text{Cap}}_k \approx C_{\text{model}} P_k + b$ yields a capacity constant $C_{\text{model}} \approx 2.16$ with a small intercept and high R^2. This smooth relationship is similar to those observed in previous literature [Roberts et al., 2020, Lu et al., 2024, Allen-Zhu and Li, 2024, Morris et al., 2025]. Our family of Transformer models stores roughly 2.16 bits of information per parameter.

5.2 Memorisation speeds

We measured the memorisation time $T_{\text{mem}}(P, n)$ for several model sizes and dataset sizes, and for each we computed the corresponding capacity fraction $f(P, n)$. Fig. 3a shows that memorisation

[2]We picked a slightly lower threshold for validation accuracy because this helped remove noise from empirical data — we observed runs where models reached 99% train accuracy and above 98% validation accuracy, but subsequently saw a large number of epochs elapse before validation accuracy matched train accuracy.



(a) Saturation time against inverse model capacity $1/(C_{\text{model}}P)$.

(b) Saturation time against capacity fraction $f(P, n_{\text{equiv}})$.

Figure 3: Memorisation speed experiments. Fig. 3a shows that memorisation time increases with inverse model capacity $1/(C_{\text{model}}P)$ across datasets; i.e. smaller models take longer to memorise. The shape of the curve varies across datasets. Fig. 3b shows that when epochs to saturation is plotted against capacity fraction, all the datasets collapse roughly onto a single curve, suggesting that memorisation speed is determined by the capacity fraction, rather than model size or dataset complexity alone.

time increases with inverse model capacity $1/C_{\text{model}P}$ across datasets; i.e. smaller models take longer to memorise. Equivalently, larger models memorise faster, corroborating previous results from Tirumala et al. [2022]. Meanwhile, Fig. 3b shows that when epochs to saturation is plotted against capacity fraction, points across all the datasets collapse roughly onto a single curve, suggesting that memorisation speed is determined by the capacity fraction, rather than model size or dataset complexity alone.

In particular, epochs until memorisation increases with capacity fraction, and we find that $T_{\text{mem}}(P) \approx be^{af}$ for some constants a, b and $f \in [0, 0.25]$. We treat this exponential as an empirical functional fit rather than a mechanistic claim; nonetheless, it provides a principled account of the previously reported observation that larger models memorise faster [Tirumala et al., 2022], by recasting it as a near-linear scaling with capacity fraction: a fixed dataset complexity occupies a smaller fraction of a larger model's capacity, and our fit then predicts faster saturation.

5.3 Generalisation delay

We trained a range of models with different internal dimensions d and primes p and recorded training and validation accuracies and losses at each epoch, allowing us to compute $E_{\text{train}}(P)$, $E_{\text{val}}(P)$, and $\Delta E(P)$. Fig. 4 shows representative training and validation curves for modular division at $p = 127$ as we vary model size.

We also plotted the generalisation delay $\Delta E(P)$ versus parameter count in Fig. 1 for several primes, allowing us to visualise the various regimes of memorisation / generalisation as a function of model size. Using Eq. (5), we compute the critical parameter count P_{mem} for the modular division datasets. We find that for several primes (including $p = 113$ and $p = 139$ shown in Fig. 1), the first models capable of achieving near-perfect training *and* test accuracy have parameter counts P slightly below but on the same order as P_{mem}, indicating that gradient descent is able to find algorithmic solutions that are more compact than the raw dataset.

Surprisingly, $\Delta E(P)$ remains at zero as model size increases for small models, even when the model has enough theoretical capacity to memorise the training set. The exact point at which $\Delta E(P)$ becomes non-zero is dependent on the prime p and the training fraction α, and is strongly correlated with the intersection of the memorisation and generalisation speeds, as we will see next in Section 5.4.

5.4 The speed intersection tracks grokking onset

For each prime p, we load the memorisation-speed experiments for matching model sizes, where we computed the memorisation time $T_{\text{mem}}(P)$ for a random dataset of the same complexity $K_{\text{mem}}(p, \alpha)$.

Table 1: Quantitative tests of the intersection hypothesis. All tests operate on $\log_{10}$ onset coordinates; p_{perm} denotes a 10 000-shuffle permutation p-value. $M_0, \ldots, M_3$ are nested OLS models with target $\log_{10} P_{\text{onset}}$: M_0 intercept-only, $M_1 = \{\log_{10} \widehat{P}_{\text{cross}}\}$, $M_2 = \{\text{dropout}\}$, $M_3 = M_1 \cup M_2$. See Section B for definitions and the residual analysis.

Sub-claim / Test	Statistic	p-value
(1) Rank predictiveness		
Spearman ρ	0.976	$p_{\text{perm}} < 10^{-3}$
Kendall τ	0.911	3.0×10^{-5}
(2) Calibration to $y = x$		
Lin's CCC (95% CI)	0.74 [0.51, 0.80]	—
Slope $\hat{b}$ (log–log OLS)	0.985	—
Intercept $\hat{a}$	-0.076	—
Joint F-test for $(a = 0, b = 1)$	$F = 199$	1.5×10^{-7}
Wilcoxon on log-residuals	median -0.16	2.0×10^{-3}
(3) Sufficiency vs. baselines (nested OLS)		
M_1 vs. M_0 (intersection has signal)	$F = 569$	1.0×10^{-8}
M_3 vs. M_2 (intersection adds over hyperparams)	$F = 498$	9.2×10^{-8}
M_3 vs. M_1 (hyperparams add over intersection)	$F \approx 0$	1.0

We plot the generalisation delay $\Delta E(P)$ and the generalisation time $T_{\text{gen}}(P)$ versus parameter count on a common x-axis. Fig. 1 shows the resulting plots for three primes. Several patterns emerge:

1. For small parameter counts, $T_{\text{gen}}(P) < T_{\text{mem}}(P)$: generalisation is faster than memorisation, and generalisation delays are zero.
2. As P increases, $T_{\text{mem}}(P)$ decreases more steeply than $T_{\text{gen}}(P)$. At a characteristic parameter count $P_{\text{cross}}(p)$ the two curves intersect.
3. Empirically, $P_{\text{cross}}(p)$ coincides closely with the onset of non-zero generalisation delay.

To assess this quantitatively, we decompose the hypothesis that the intersection of T_{mem} and T_{gen} predicts the empirical grokking onset into three falsifiable sub-claims — predictiveness, calibration to $y = x$, and sufficiency against baselines — and report a test for each (Table 1); a fourth, robustness across swept axes, is part of the suite (Section B) but inconsequential on the central sweep where dropout is fixed. The rank order of predicted and empirical onsets is essentially perfect (Spearman $\rho = 0.976$, permutation $p < 10^{-3}$); the log–log slope is 0.985, indicating no proportional bias; and the predicted onset is a sufficient statistic against the swept hyperparameter (dropout): given $\widehat{P}_{\text{cross}}$, dropout adds no further explanatory power over the intersection alone ($F \approx 0$, $p = 1$). The only residual is a small, prime-independent constant offset — empirical onset arrives roughly 30% earlier than predicted (median $\log_{10}(P_{\text{onset}}/\widehat{P}_{\text{cross}}) = -0.16$) — so the intersection captures the scaling of the onset with the prime exactly, up to a single multiplicative correction. Full test definitions and per-model regression numbers are deferred to Section B.

Taken together, these results provide evidence that grokking appears when model memorisation speed is roughly equal to generalisation speed. The data suggest that there are three learning regimes in grokking modular division as model size increases. We start at the underfitting regime: when $P \ll P_{\text{mem}}(p, \alpha)$, the model does not have enough capacity to memorise either the training set or the algorithmic solution, so it achieves low training accuracy and generalisation. As P approaches $P_{\text{mem}}(p, \alpha)$ but does not exceed it, generalisation follows immediately from strong training accuracy because the model does not have enough capacity to memorise the entire training set, so a low training loss must be achieved through algorithmic generalisation. As P continues to increase past $P_{\text{mem}}(p, \alpha)$, the model does not default to memorising the training set initially (even though it has enough capacity to do so), because $T_{\text{mem}}(P) \gg T_{\text{gen}}(P)$, so gradient descent settles upon the quicker-to-find, algorithmic solution, and we remain in the immediate generalisation regime. Finally, as P continues to increase past the intersection point $P_{\text{cross}}(p)$, the model prefers memorising when $T_{\text{mem}}(P) \lesssim T_{\text{gen}}(P)$, so gradient descent finds the memorisation solution first before generalising, leading to delayed generalisation (i.e. 'grokking').

Robustness to other hyperparameters, architectures, and tasks. The central sweep above fixes every hyperparameter except the prime p and the embedding width d. We test the framework's robustness to other settings in six further suites: a weight-decay sweep (Section C.2), a learning-rate sweep (Section C.3), an initialisation-scale sweep (Section C.1), and a training-fraction sweep (Section C.4); a depth-scaling sweep (Section D.1); and a modular-addition task sweep (Section E.1). Across all six, our framework holds within any one consistent setting of hyperparameter, architecture, and task; analysing how the framework calibrates across settings is a separate question we leave for future work.

6 Discussion

Together our results give a mechanistic account of how model capacity controls grokking on modular arithmetic, by setting the relative speeds of two learning processes.

Capacity acts on grokking through learning speeds, not the capacity threshold. A natural reading of bits-per-parameter capacity [Morris et al., 2025] is a threshold prediction: grokking begins when $C_{\text{model}}P \gtrsim K_{\text{mem}}$, since only then is the memorising solution representable. Our data show that this is not what happens for modular division. For several primes the smallest models that achieve near-perfect train and test accuracy already have $P \lesssim P_{\text{mem}}$, indicating that gradient descent can find an algorithmic solution more compact than the raw lookup; and over an extended range of $P > P_{\text{mem}}$ the models continue to generalise immediately, with no grokking delay. The transition into the grokking regime instead coincides with the parameter count at which the measured $T_{\text{mem}}(P)$ and $T_{\text{gen}}(P)$ curves cross — a count strictly larger than P_{mem}. What controls whether a model groks is not whether the lookup is representable, but whether it is reached before the algorithmic solution.

Connection to existing accounts. Our work refines existing accounts that frame grokking as a competition between memorising and generalising solutions [Varma et al., 2023, Merrill et al., 2023, Huang et al., 2024, Kumar et al., 2024]: previous works identify which solution is preferred at convergence, while we give a more formal treatment on which solution gradient descent encounters first as a function of model capacity. The qualitative 'small models do not grok' regime documented in Liu et al. [2022a] and Huang et al. [2024] is recovered as the regime $T_{\text{gen}}(P) < T_{\text{mem}}(P)$. Our framing also formalises the speed intuition of Davies et al. [2023], replacing a generic 'different patterns are learned at different rates' picture with two concrete, separately measurable timescales whose intersection tracks the empirical phase boundary.

Recovering the larger-models-memorise-faster observation. On random-label data, memorisation time depends primarily on the capacity fraction $f = K/(C_{\text{model}}P)$ rather than on P or K separately (Fig. 3b), with empirical fit $T_{\text{mem}} \propto e^{af}$ for $f \in [0, 0.25]$. For fixed K, larger P then memorises faster, recovering the qualitative observation of Tirumala et al. [2022] as a near-linear scaling in capacity fraction. The exponential is an empirical functional form, however, rather than a derived theorem.

Scope, limitations, and outlook. The framework is mechanistic rather than architecture-agnostic-predictive: $T_{\text{gen}}(P)$ is measured rather than derived, so a new architecture or task requires re-running the speed measurements. We additionally test robustness to weight decay, learning rate, initialisation scale, and the training fraction α (Section C), to depth (Section D), and to modular addition in place of division (Section E). Within each fixed setting the framework's within-setting predictiveness is preserved, while the calibration constant shifts smoothly across settings: it recalibrates with weight decay, with depth, and with the training fraction α, more weakly with initialisation scale, and remains essentially flat across learning rate within the optimisation regime where speed itself is well-defined. Sensitivity to dropout and to the number of attention heads, as well as to architectural variants beyond the gated decoder-only Transformer (e.g. ungated FFNs, LayerNorm in place of RMSNorm, learned positional embeddings, MLP baselines), remains future work, as is whether similar speed-capacity trade-offs apply to larger models and naturalistic tasks. The broader takeaway is that for grokking on modular arithmetic, what determines onset is not the static capacity threshold alone but the relative speeds of memorisation and generalisation as functions of model capacity, an abstraction we hope will prove useful for the study of delayed generalisation beyond this setting.

References

Zeyuan Allen-Zhu and Yuanzhi Li. Physics of language models: Part 3.3, knowledge capacity scaling laws. *arXiv preprint arXiv:2404.05405*, 2024.

Devansh Arpit, Stanisław Jastrzębski, Nicolas Ballas, David Krueger, Emmanuel Bengio, Maxinder S Kanwal, Tegan Maharaj, Asja Fischer, Aaron Courville, Yoshua Bengio, et al. A closer look at memorization in deep networks. In *International conference on machine learning*, pages 233–242. PMLR, 2017.

Nicholas Carlini, Daphne Ippolito, Matthew Jagielski, Katherine Lee, Florian Tramer, and Chiyuan Zhang. Quantifying memorization across neural language models. In *The Eleventh International Conference on Learning Representations*, 2023. URL `https://openreview.net/forum?id=TatRHT_1cK`.

Kenzo Clauw, Sebastiano Stramaglia, and Daniele Marinazzo. Information-theoretic progress measures reveal grokking is an emergent phase transition. *arXiv preprint arXiv:2408.08944*, 2024.

Xander Davies, Lauro Langosco, and David Krueger. Unifying grokking and double descent. *arXiv preprint arXiv:2303.06173*, 2023.

Branton DeMoss, Silvia Sapora, Jakob Foerster, Nick Hawes, and Ingmar Posner. The complexity dynamics of grokking. *Physica D: Nonlinear Phenomena*, page 134859, 2025.

Hiroki Furuta, Gouki Minegishi, Yusuke Iwasawa, and Yutaka Matsuo. Towards empirical interpretation of internal circuits and properties in grokked transformers on modular polynomials. *arXiv preprint arXiv:2402.16726*, 2024.

Tianyu He, Darshil Doshi, Aritra Das, and Andrey Gromov. Learning to grok: Emergence of in-context learning and skill composition in modular arithmetic tasks. In *ICML 2024 Workshop on Mechanistic Interpretability*.

Yufei Huang, Shengding Hu, Xu Han, Zhiyuan Liu, and Maosong Sun. Unified view of grokking, double descent and emergent abilities: A perspective from circuits competition. *arXiv preprint arXiv:2402.15175*, 2024.

Ahmed Imtiaz Humayun, Randall Balestriero, and Richard Baraniuk. Deep networks always grok and here is why. In *Forty-first International Conference on Machine Learning*, 2024. URL `https://openreview.net/forum?id=zMue490KMr`.

Tanishq Kumar, Blake Bordelon, Samuel Gershman, and Cengiz Pehlevan. Grokking as the transition from lazy to rich training dynamics. In *International Conference on Learning Representations*, volume 2024, pages 23010–23035, 2024.

Jaerin Lee, Bong Gyun Kang, Kihoon Kim, and Kyoung Mu Lee. Grokfast: Accelerated grokking by amplifying slow gradients. *arXiv preprint arXiv:2405.20233*, 2024.

Ziming Liu, Ouail Kitouni, Niklas S Nolte, Eric Michaud, Max Tegmark, and Mike Williams. Towards understanding grokking: An effective theory of representation learning. *Advances in Neural Information Processing Systems*, 35:34651–34663, 2022a.

Ziming Liu, Eric J Michaud, and Max Tegmark. Omnigrok: Grokking beyond algorithmic data. *arXiv preprint arXiv:2210.01117*, 2022b.

Ilya Loshchilov and Frank Hutter. Decoupled weight decay regularization. *arXiv preprint arXiv:1711.05101*, 2017.

Xingyu Lu, Xiaonan Li, Qinyuan Cheng, Kai Ding, Xuan-Jing Huang, and Xipeng Qiu. Scaling laws for fact memorization of large language models. In *Findings of the Association for Computational Linguistics: EMNLP 2024*, pages 11263–11282, 2024.

Kaifeng Lyu, Jikai Jin, Zhiyuan Li, Simon Du, Jason Lee, and Wei Hu. Dichotomy of early and late phase implicit biases can provably induce grokking. In *International Conference on Learning Representations*, volume 2024, pages 33897–33936, 2024.

Shalima Binta Manir and Anamika Paul Rupa. A systematic empirical study of grokking: Depth, architecture, activation, and regularization. *arXiv preprint arXiv:2603.25009*, 2026.

William Merrill, Nikolaos Tsilivis, and Aman Shukla. A tale of two circuits: Grokking as competition of sparse and dense subnetworks. 2023. URL https://openreview.net/forum?id=8GZxtu46Kx.

Mohamad Amin Mohamadi, Zhiyuan Li, Lei Wu, and Danica J. Sutherland. Why do you grok? A theoretical analysis on grokking modular addition. In *Proceedings of the 41st International Conference on Machine Learning*, volume 235 of *Proceedings of Machine Learning Research*, pages 35934–35967. PMLR, 2024.

John X Morris, Chawin Sitawarin, Chuan Guo, Narine Kokhlikyan, G Edward Suh, Alexander M Rush, Kamalika Chaudhuri, and Saeed Mahloujifar. How much do language models memorize? *arXiv preprint arXiv:2505.24832*, 2025.

Preetum Nakkiran, Gal Kaplun, Yamini Bansal, Tristan Yang, Boaz Barak, and Ilya Sutskever. Deep double descent: Where bigger models and more data hurt. In *International Conference on Learning Representations*, 2020. URL https://openreview.net/forum?id=B1g5sA4twr.

Neel Nanda, Lawrence Chan, Tom Lieberum, Jess Smith, and Jacob Steinhardt. Progress measures for grokking via mechanistic interpretability. 2023. URL https://openreview.net/forum?id=9XFSbDPmdW.

Alethea Power, Yuri Burda, Harri Edwards, Igor Babuschkin, and Vedant Misra. Grokking: Generalization beyond overfitting on small algorithmic datasets. *arXiv preprint arXiv:2201.02177*, 2022.

Adam Roberts, Colin Raffel, and Noam Shazeer. How much knowledge can you pack into the parameters of a language model? In *Proceedings of the 2020 conference on empirical methods in natural language processing (EMNLP)*, pages 5418–5426, 2020.

Noa Rubin, Inbar Seroussi, and Zohar Ringel. Grokking as a first order phase transition in two layer networks. *arXiv preprint arXiv:2310.03789*, 2023.

Vimal Thilak, Etai Littwin, Shuangfei Zhai, Omid Saremi, Roni Paiss, and Joshua Susskind. The slingshot mechanism: An empirical study of adaptive optimizers and the grokking phenomenon. *arXiv preprint arXiv:2206.04817*, 2022.

Kushal Tirumala, Aram Markosyan, Luke Zettlemoyer, and Armen Aghajanyan. Memorization without overfitting: Analyzing the training dynamics of large language models. *Advances in Neural Information Processing Systems*, 35:38274–38290, 2022.

Vikrant Varma, Rohin Shah, Zachary Kenton, János Kramár, and Ramana Kumar. Explaining grokking through circuit efficiency. *arXiv preprint arXiv:2309.02390*, 2023.

Boshi Wang, Xiang Yue, Yu Su, and Huan Sun. Grokked transformers are implicit reasoners: A mechanistic journey to the edge of generalization. *arXiv preprint arXiv:2405.15071*, 2024.

Chiyuan Zhang, Samy Bengio, Moritz Hardt, Benjamin Recht, and Oriol Vinyals. Understanding deep learning requires rethinking generalization. In *International Conference on Learning Representations (ICLR)*, 2017. URL https://arxiv.org/abs/1611.03530.

A Experiment details

A.1 Modular division dataset

We use all 10 primes in the range from 90 to 140 for our experiments: i.e. 97, 101, 103, 107, 109, 113, 127, 131, 137, 139.

A.2 Architecture and optimisation

All experiments in the central sweep train decoder-only Transformers in PyTorch using AdamW with learning rate 10^{-3}, betas $(0.9, 0.98)$, weight decay 1.0, and batch size 512, for a maximum of $5{,}000$ epochs. We fix depth $L_{\text{depth}} = 2$ and a single attention head $H = 1$, varying model size by changing the embedding width d. Dropout is 0.2 in grokking and speed runs and 0 in capacity runs.

A.3 Compute resources

All experiments were run on NVIDIA A100 and H100 GPUs, with each training run occupying a single GPU. Runs were dispatched in parallel across available GPUs via a YAML-configured job scheduler (`gc-dispatch`); per-run wall-clock time is recorded in the run registry. The full set of capacity, speed, and grokking experiments reported here required on the order of 10^3 GPU-hours in aggregate; preliminary and discarded sweeps used a comparable additional amount.

A.4 Estimating capacity on random data

For each model dimension $d \in \{10, 12, 14, 16, 18, 20, 22\}$ and dataset size $n \in \{1000,\ 1374,\ 1891,\ 2601,\ 3576,\ 4917,\ 6761,\ 9300\}$ we generate a random dataset $(X_{\text{train}}, T_{\text{train}})$ of size n, sampling each token and target uniformly from the vocabulary of size $V = p + 2$ at $p = 113$. We instantiate a Transformer of width d and train it as in Section A.2, except with dropout 0, stopping when the training loss fails to improve by more than $\Delta = 10^{-4}$ for a patience window of 100 epochs. We compute the total memorisation M_T via Eq. (2) and the bits memorised per example $m_T = M_T/n$. Within-arch capacity curves are stable across seeds in our setting, so we use a single seed (42) per cell. Fig. 2 (left) shows the resulting $M_T(n)$ for several model sizes.

A.5 Measuring memorisation speeds on random data

For each prime p in the 10-prime sweep (Section A) and each model dimension $d \in \{20, 24, 28, \ldots, 256\}$ (44 widths in $\{20, 24, \ldots, 128\} \cup \{136, 144, \ldots, 256\}$), we generate a random-label dataset of size $n_{\text{equiv}}(p, \alpha) = K_{\text{mem}}(p, \alpha)/\log_2 V$. We instantiate a Transformer of width d and train it as in Section A.2 (dropout 0.2, weight decay 1.0), recording training accuracy at each epoch. We declare saturation once training accuracy first exceeds 99%, and report $T_{\text{mem}}(P)$ as the average of the saturation epoch over 10 seeds (seeds 42–51).

A.6 Grokking experiments on modular division

For each prime p in the 10-prime sweep and each model dimension $d \in \{20, 22, 24, \ldots, 128\} \cup \{130, 140, 150, \ldots, 1000\}$ (truncated to $d \leq 256$ when fed into the per-prime intersection figures via `max_dim`), we construct a modular-division dataset $(X_{\text{train}}, T_{\text{train}}, X_{\text{test}}, T_{\text{test}})$ with training fraction $\alpha = 0.5$ and a random train–test split. We instantiate a Transformer of width d and train it as in Section A.2 (dropout 0.2, weight decay 1.0), recording training and validation accuracies and losses at each epoch. We use 10 seeds per cell (seeds 42–51); $T_{\text{gen}}(P)$ is reported as the mean and $\Delta E(P)$ as the per-seed minimum, as defined in Section 4.3.

Fig. 4 shows representative training and validation curves for modular division at $p = 127$ as we vary model size.

A.7 Hyperparameter, architectural, and task sweeps beyond the central setting

Beyond the central sweep, we run analogous `capacity` → `speed` → `groks` pipelines under varied hyperparameters, varied architectural axes, and varied modular-arithmetic tasks. Each sweep reuses the architecture, optimiser, dataset construction, and aggregation conventions of Sections A.2 and A.4 to A.6; only the swept axis is changed and any data-dependent quantities (e.g. K_{mem}, n_{equiv}) are recomputed. For the depth sweep, dim is selected per cell to hit fixed parameter-count targets rather than chosen directly. For the training-fraction sweep, n_{equiv} is recomputed per α on the speed side while the architecture (and hence the bits-per-parameter constant inherited from the matched arch group) is held fixed. Per-axis settings, headline figures, and statistical tests are reported in Section C (hyperparameter invariance), Section D (architectural invariance), and Section E (task invariance).

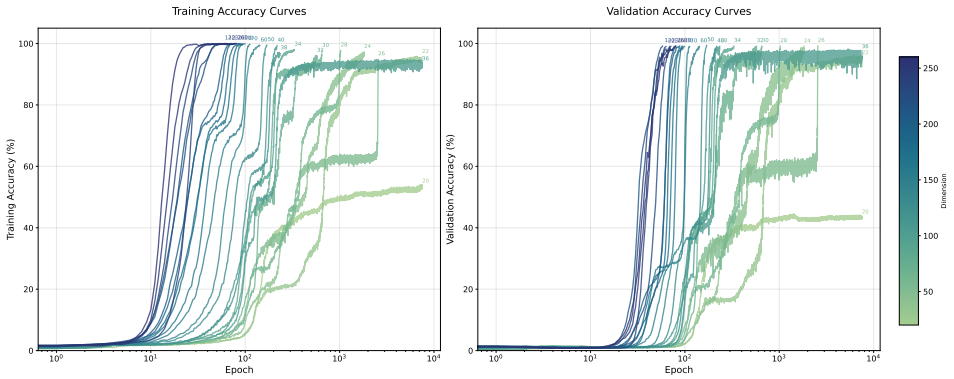


Figure 4: Training (left) and validation (right) accuracy curves for modular division with $p = 127$ across model sizes. Small models underfit, intermediate models generalise immediately, and larger models exhibit grokking.

B Quantitative tests of the intersection hypothesis

We turn the qualitative claim "the intersection of T_{mem} and T_{gen} predicts the empirical grokking onset" into three falsifiable sub-claims and report a test for each. All tests operate on $\{(\widehat{P}_{\text{cross}}(p),\ P_{\text{onset}}(p))\}_p$ in $\log_{10}$ coordinates, where $\widehat{P}_{\text{cross}}(p)$ is the parameter count at which the seed-averaged T_{mem} and T_{gen} curves cross, and $P_{\text{onset}}(p)$ is the smallest model size P for which $\Delta E(P') > 0$ across seeds for every $P' > P$.

Predictiveness. We test for any monotone relationship between predicted and empirical onsets via Spearman's ρ (with both an analytic p-value and a 10^4-shuffle permutation p-value, the latter to guard against optimistic analytic tails at small N) and Kendall's τ (different small-N tail behaviour to Spearman). Both pass with $\rho = 0.976$ and $\tau = 0.911$.

Calibration. Rank correlation alone does not commit to $\hat{e} \approx \hat{p}$: a strongly correlated predictor with the wrong slope or a constant offset can pass predictiveness but fail calibration. We test calibration with three statistics:

- Lin's concordance correlation coefficient $\text{CCC} = 2\rho\sigma_p\sigma_e/(\sigma_p^2+\sigma_e^2+(\mu_p-\mu_e)^2)$, the natural one-number summary of "predicted equals empirical" since it penalises both decorrelation and offset from $y = x$. We report a 95% bootstrap CI from 10^4 cell-level resamples.
- OLS fit $\log_{10} P_{\text{onset}} = a + b \log_{10} \widehat{P}_{\text{cross}}$ with a joint F-test for $(a = 0, b = 1)$. Reporting $(\hat{a}, \hat{b})$ separately makes the *direction* of any miss legible: a slope < 1 means the predictor over-extrapolates large onsets, an intercept > 0 means it systematically under-predicts.
- Wilcoxon signed-rank on the log-residuals $\log_{10}(P_{\text{onset}}/\widehat{P}_{\text{cross}})$ against zero, which tests for symmetric bias and is robust to outliers in a way the joint F-test is not.

On the central sweep, the slope is $\hat{b} = 0.985$ (no proportional bias) and the intercept $\hat{a} = -0.076$, but the data are tight enough that the joint F-test still rejects $(0, 1)$ ($F = 199$, $p = 1.5 \times 10^{-7}$). The Wilcoxon test confirms a small symmetric bias (median log-residual -0.16, $p = 2 \times 10^{-3}$). The OLS intercept and the Wilcoxon median are not in tension: the residual model $\log_{10} P_{\text{onset}} \approx -0.076 + 0.985 \log_{10} \widehat{P}_{\text{cross}}$, evaluated at typical onset values $\log_{10} \widehat{P}_{\text{cross}} \approx 5$, gives a per-cell offset $\log_{10}(P_{\text{onset}}/\widehat{P}_{\text{cross}}) \approx -0.076 - 0.015 \cdot 5 \approx -0.15$, in line with the median log-residual. We interpret this as a single ~ 0.16 dex constant offset rather than a structural miscalibration: the predictor scales correctly with p but over-estimates absolute onset by $\sim 30\%$.

Sufficiency vs. baselines. The strongest version of the claim is that the intersection is a sufficient statistic for the empirical onset, in the sense that no simpler predictor does as well. We operationalise this with nested OLS comparisons against $\log_{10} P_{\text{onset}}$:

M_0 **(null):** intercept only.

M_1 **(intersection):** $\log_{10} \widehat{P}_{\text{cross}}$.

M_2 **(hyperparams):** every column in the config's swept axes (here, dropout).

M_3 **(combined):** $M_1 \cup M_2$ predictors.

M_1 vs. M_0 confirms that the intersection has any signal at all. M_3 vs. M_2 confirms that the intersection adds information *over and above* the swept hyperparameters — this is the test for the sceptic who claims the correlation is spurious because both onset and intersection depend on p. M_3 vs. M_1 is the sufficiency test proper: do the hyperparameters add anything beyond the intersection? On the central sweep, RSS values give in-sample / adjusted R^2: $M_0 = 0$, $M_1 = 0.986/0.984$, $M_2 = 0/-0.125$, $M_3 = 0.986/0.982$. The corresponding F-tests (Table 1) reject M_0 in favour of M_1 ($F = 569$, $p = 10^{-8}$) and M_2 in favour of M_3 ($F = 498$, $p = 9 \times 10^{-8}$), but the upgrade from M_1 to M_3 is statistically and numerically null ($F \approx 0$, $p = 1$): given $\widehat{P}_{\text{cross}}$, dropout adds no further explanatory power.

Robustness. For configurations with multiple swept axes we additionally regress the per-cell log-residual against each axis and Holm-correct the resulting p-values across axes. The intent is to flag systematic mispredictions along any axis (e.g. residuals trending with weight decay or depth). The robustness sub-claim is inconsequential in the central sweep, where dropout is fixed within each grokking cell.

What this is not. The setup above is not a power analysis: with ~ 10 cells per figure, only large effects are detectable, and the point is to prevent overclaiming from underpowered data, not to certify the predictor as perfect. It is also not cross-validated: with this N, k-fold leaves 5–6 training points per fold and variance dominates bias, so the nested-model F-tests use in-sample fits and report adjusted R^2 as the honest version of the comparison. Finally, it is not a hierarchical model: each cell is one observation, and per-seed variability is folded into the seed-min onset estimate via the aggregation procedure of Section 5.3 rather than modelled explicitly.

C Hyperparameter invariance

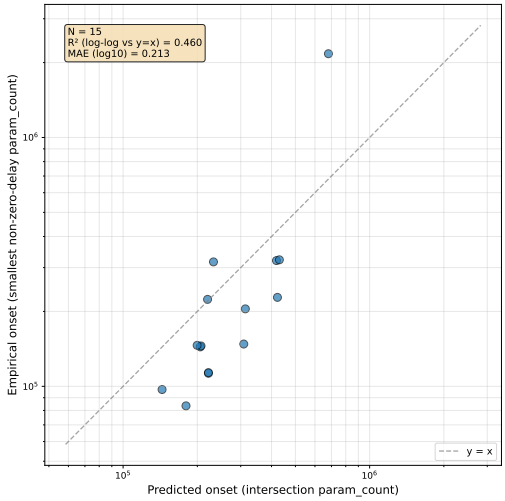
Scope and reading guide. The central sweep (Section 5.4) fixes every hyperparameter except the prime p and the embedding width d. To assess robustness, we re-run the full `capacity` → `speed` → `groks` pipeline at each setting of a swept hyperparameter and apply the statistical framework of Section B. The framework's central claim — that within a fixed hyperparameter and task setting, the parameter count at which $T_{\text{mem}}(P)$ and $T_{\text{gen}}(P)$ cross predicts the onset of grokking — does not require a single calibration constant to apply across settings. A different optimisation regime (e.g. a different initialisation scale) can shift the multiplicative offset between $\widehat{P}_{\text{cross}}$ and P_{onset} while leaving within-setting predictiveness intact. We therefore evaluate each sweep on two separate questions:

1. **Within-setting predictiveness.** Holding the swept hyperparameter fixed, do predicted and empirical onsets track across primes, and is the per-cell log-residual stable?
2. **Cross-setting calibration.** Pooling all cells, does the swept hyperparameter act as a smooth multiplicative offset, or does it interact with the predictor's slope?

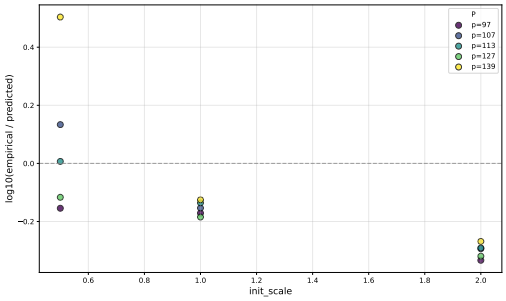
Each subsection below follows a fixed template: a *Scope* paragraph; headline figures (predicted-vs-empirical scatter and residual-vs-axis plot); a *Pooled tests* table reusing the schema of Table 1; a *Within-setting* table summarising per-cell log-residuals; and a *Verdict* paragraph that addresses both questions above. New hyperparameter sweeps slot in as additional subsections without altering the surrounding structure.

C.1 Initialisation scale

Scope. `init_scale`$\in \{0.5, 1.0, 2.0\}$, applied as a post-initialisation multiplicative scaling of all weights; all other hyperparameters as in Section A.2. Five primes per cell ($p \in \{97, 107, 113, 127, 139\}$); 10 seeds per cell; intersection finder and onset definitions identical to Section 5.4. `init_scale`$= 1.0$ matches the central sweep and serves as an in-sweep baseline.



(a) Predicted vs. empirical onset, points coloured by `init_scale`.



(b) Per-cell log-residual against `init_scale`.

Figure 5: Initialisation-scale sweep: predicted-vs-empirical scatter and residual trend with the swept axis.

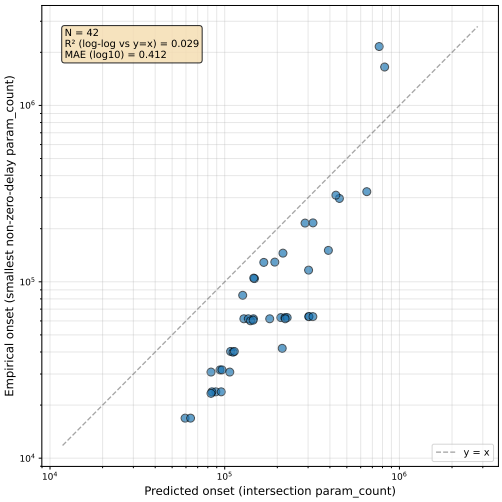
Table 2: Initialisation-scale sweep: pooled hypothesis tests on the 15 cells (5 primes $\times$ 3 `init_scale` values, $\circ = /$). Schema as in Table 1; the robustness row regresses the per-cell log-residual against $\log_2$`init_scale`.

Sub-claim / Test	Statistic	p-value
(1) Rank predictiveness		
Spearman ρ	0.839	$p_{\text{perm}} = 10^{-4}$
Kendall τ	0.676	2.0×10^{-4}
(2) Calibration to $y = x$		
Lin's CCC (95% CI)	0.622 [0.28, 0.71]	—
Slope $\hat{b}$ (log–log OLS)	1.583	—
Intercept $\hat{a}$	-3.290	—
Joint F-test for $(a = 0, b = 1)$	$F = 5.29$	0.021
Wilcoxon on log-residuals	median -0.154	0.022
(3) Sufficiency vs. baselines (nested OLS)		
M_1 vs. M_0 (intersection has signal)	$F = 30.7$	9.5×10^{-5}
M_3 vs. M_2 (intersection adds over hyperparams)	$F = 52.0$	1.1×10^{-5}
M_3 vs. M_1 (hyperparams add over intersection)	$F = 14.3$	2.6×10^{-3}
(4) Robustness across the swept axis		
`init_scale` (numeric)	slope $= -0.236$/unit	0.0031

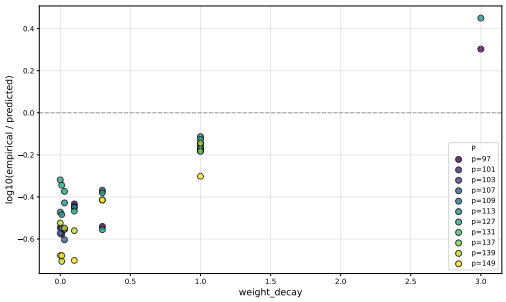
Verdict. Within `init_scale`$\in \{1.0, 2.0\}$, log-residuals are tight across primes ($\sigma_{\log} \leq 0.03$, Table 3): the predictor scales correctly with p and incurs only a constant multiplicative offset within each setting. The `init_scale`$= 1.0$ row reproduces the central-sweep result at the same five primes, with per-prime log-residuals $\{-0.17, -0.15, -0.14, -0.18, -0.13\}$. Within `init_scale`$= 0.5$ the residual variance is markedly larger, driven primarily by $p = 139$ where the empirical onset arrives at $\sim 2.2 \times 10^6$ parameters versus a predicted $\sim 6.8 \times 10^5$ — consistent with the small-init regime entering an under-trained corner where speed measurements are noisier. Across the pooled sweep, predictiveness is preserved ($\rho = 0.839$), and the calibration constant trends monotonically with `init_scale` (-0.24 dex per unit, $p = 0.003$). We read this as a smooth setting-specific recalibration of the predictor rather than a structural failure: the predictor still ranks correctly, and within `init_scale`$\in \{1.0, 2.0\}$ the per-cell offset is stable.

Table 3: Initialisation-scale sweep: within-setting log-residual summary across the 5 primes. Tight per-cell standard deviations indicate that the predictor scales correctly with p at each fixed setting.

`init_scale`	n_{primes}	median $\log_{10}(P_{\text{onset}}/\widehat{P}_{\text{cross}})$	std	within-setting verdict
0.5	5	$+0.007$	0.260	weak (driven by $p = 139$)
1.0	5	-0.154	0.024	strong
2.0	5	-0.294	0.026	strong



(a) Predicted vs. empirical onset, points coloured by `weight_decay`.



(b) Per-cell log-residual against `weight_decay`.

Figure 6: Weight-decay sweep: predicted-vs-empirical scatter and residual trend with the swept axis.

C.2 Weight decay

Scope. `weight_decay`$\in \{0, 0.01, 0.03, 0.1, 0.3, 1.0, 3.0\}$, matched between the speed and grokking runs. Six primes per cell ($p \in \{97, 107, 113, 127, 139, 149\}$, with the central-sweep $\{101, 103, 109, 131, 137\}$ also present at λ=1.0 for continuity); 5 seeds per cell except the λ=1.0 baseline cells, which inherit the central sweep's seed pool; intersection finder and onset definitions identical to Section 5.4. `weight_decay`$= 1.0$ matches the central sweep and serves as an in-sweep baseline; λ=3.0 pushes most cells beyond the explored width range and so contributes only partial cells (2/6 onsets recorded at λ=3.0). Capacity is re-measured at $\lambda \in \{0.01, 0.1, 1.0\}$ and pinned at $C_{\text{model}} = 2.16$ when no matching capacity cell exists.

Verdict. Within-setting predictiveness is best at λ=1.0 (the central-sweep regime) and degrades smoothly as λ moves away from this baseline: the per-cell offset becomes more negative at small λ (the predictor over-shoots empirical onset, increasingly so as decay weakens) and turns positive at λ=3.0. The across-axis robustness regression captures this monotonically: each unit increase in λ shifts the log-residual by $+0.32$ dex (p=10^{-18}). Pooled rank predictiveness remains high ($\rho = 0.900$), and the intersection adds substantial information over λ alone (M_3 vs. M_2, F=167), but the sceptic-friendly M_3 vs. M_1 comparison rejects: λ *does* add information beyond the intersection here. We read this as the predictor recalibrating with λ rather than transferring as a single offset, consistent with weight decay reshaping the speed curves rather than just translating them. The qualitative claim that the intersection tracks grokking onset is preserved at every λ where both curves are well-resolved, but a λ-aware calibration is required for cross-setting comparisons.

C.3 Learning rate

Scope. `lr`$\in \{10^{-4}, 3\times10^{-4}, 10^{-3}, 3\times10^{-3}, 10^{-2}\}$, matched between the speed and grokking runs. Five primes per cell ($p \in \{97, 107, 113, 127, 139\}$); 4 seeds per cell; all other hyperparameters

Table 4: Weight-decay sweep: pooled hypothesis tests on the 42 valid cells (out of 47; the missing 5 cells are at $\lambda \in \{0.03, 3.0\}$ where empirical onset lies above the swept width range). Schema as in Table 1; the robustness row regresses the per-cell log-residual against λ.

Sub-claim / Test	Statistic	p-value
(1) Rank predictiveness		
Spearman ρ	0.900	$p_{\text{perm}} = 10^{-4}$
Kendall τ	0.774	9.8×10^{-13}
(2) Calibration to $y = x$		
Lin's CCC (95% CI)	0.531 [0.35, 0.65]	—
Slope $\hat{b}$ (log–log OLS)	1.439	—
Intercept $\hat{a}$	-2.683	—
Joint F-test for $(a = 0, b = 1)$	$F = 72.4$	5.1×10^{-14}
Wilcoxon on log-residuals	median -0.431	2.0×10^{-9}
(3) Sufficiency vs. baselines (nested OLS)		
M_1 vs. M_0 (intersection has signal)	$F = 150$	4.0×10^{-15}
M_3 vs. M_2 (intersection adds over hyperparams)	$F = 167$	1.8×10^{-15}
M_3 vs. M_1 (hyperparams add over intersection)	$F = 92.0$	2.7×10^{-15}
(4) Robustness across the swept axis		
weight_decay (numeric)	slope $= +0.321$/unit λ	1.9×10^{-18}

Table 5: Weight-decay sweep: within-setting log-residual summary across primes. Rows with fewer than 5 primes have onsets above the explored width range at the missing cells.

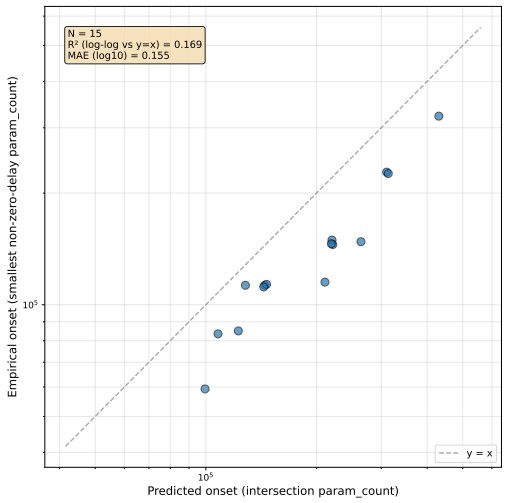
`weight_decay`	n_{primes}	median $\log_{10}(P_{\text{onset}}/\widehat{P}_{\text{cross}})$	std	within-setting verdict
0.0	6	-0.535	0.119	weak (residuals widen at small λ)
0.01	6	-0.564	0.131	weak
0.03	5	-0.548	0.096	moderate
0.1	6	-0.458	0.105	moderate
0.3	6	-0.415	0.082	moderate
1.0	11	-0.171	0.049	strong
3.0	2	$+0.376$	0.105	under-resolved (4/6 cells above the width range)

as in Section A.2. `lr`$= 10^{-3}$ matches the central sweep and serves as an in-sweep baseline. The two largest learning rates do not produce grokking within the explored width range ($d \leq 256$): at `lr`$= 3\times10^{-3}$ the predictor still emits a finite $\widehat{P}_{\text{cross}}$ but no empirical onset is recorded within 5,000 epochs, and at `lr`$= 10^{-2}$ training does not reach saturation on either random or modular data. Pooled tests therefore operate on the 15 cells from the lower three learning rates.

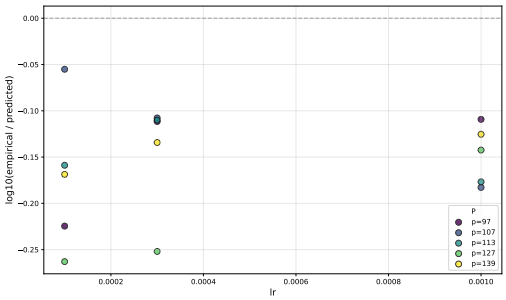
Verdict. Across the three learning rates that produce grokking, within-setting predictiveness is preserved: per-cell log-residuals are tight ($\sigma_{\log} \leq 0.08$), the predictor ranks the five primes correctly at every fixed η, and the calibration constant is essentially flat as a function of η (across-axis slope statistically null, p=0.62). Pooled rank predictiveness is excellent (ρ=0.972), and the sufficiency comparison passes: given $\widehat{P}_{\text{cross}}$, η adds no further explanatory power (M_3 vs. M_1, F=0.98, p=0.34). Outside this regime, we observe two qualitatively distinct failure modes: at η=3×10^{-3} the predictor extrapolates a $\widehat{P}_{\text{cross}}$ in the 10^6-parameter range but no model in the swept width range groks within the epoch budget, and at η=10^{-2} training never reaches saturation on either random or modular data. Both regimes lie outside the optimisation window where the speed measurements themselves are well-defined, and we treat them as out-of-scope rather than as predictor failures.

C.4 Training fraction

Scope. `train_fraction`$\in \{0.3, 0.4, 0.5, 0.6, 0.7\}$, applied to the modular-division dataset; for each α the random-label dataset size used by the speed run is recomputed via $n_{\text{equiv}}(p, \alpha) = K_{\text{mem}}(p, \alpha)/\log_2 V$. Five primes per cell ($p \in \{97, 107, 113, 127, 139\}$); 4 seeds per cell, except the



(a) Predicted vs. empirical onset, points coloured by `lr`.



(b) Per-cell log-residual against `lr`.

Figure 7: Learning-rate sweep: predicted-vs-empirical scatter and residual trend with the swept axis.

Table 6: Learning-rate sweep: pooled hypothesis tests on the 15 cells (5 primes $\times$ 3 valid `lr` values). Schema as in Table 1; the robustness row regresses the per-cell log-residual against η.

Sub-claim / Test	Statistic	p-value
(1) Rank predictiveness		
Spearman ρ	0.972	$p_{\text{perm}} = 10^{-4}$
Kendall τ	0.900	3.2×10^{-6}
(2) Calibration to $y = x$		
Lin's CCC (95% CI)	0.699 [0.45, 0.81]	—
Slope $\hat{b}$ (log–log OLS)	0.942	—
Intercept $\hat{a}$	0.150	—
Joint F-test for $(a = 0, b = 1)$	$F = 51.8$	6.4×10^{-7}
Wilcoxon on log-residuals	median -0.142	6.1×10^{-5}
(3) Sufficiency vs. baselines (nested OLS)		
M_1 vs. M_0 (intersection has signal)	$F = 127$	4.4×10^{-8}
M_3 vs. M_2 (intersection adds over hyperparams)	$F = 86.3$	7.9×10^{-7}
M_3 vs. M_1 (hyperparams add over intersection)	$F = 0.98$	0.342
(4) Robustness across the swept axis		
lr (numeric)	slope $= +20.4$/unit η	0.62

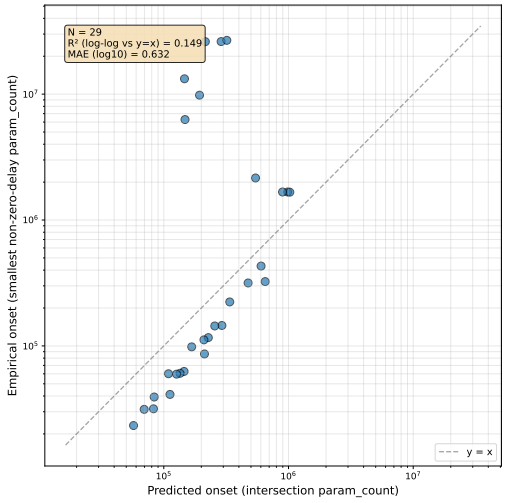
$\alpha = 0.5$ cells, which inherit the central sweep's full seed pool and 11-prime grid.[3] Intersection finder, onset definitions, and `max_dim`$= 256$ as in Section 5.4. `train_fraction`$= 0.5$ matches the central sweep and serves as an in-sweep baseline. No new capacity runs are required: changing α alters the dataset complexity but not the architecture, so C_{model} is reused from the matched arch group (λ=1.0, dropout$= 0.2$).

Verdict. Within each fixed α the predictor ranks the five (or eleven, at α=0.5) primes essentially correctly: per-cell log-residuals are tight at $\alpha \in \{0.3, 0.4, 0.5\}$ ($\sigma_{\log} \leq 0.05$, Table 9). The residual spread widens at $\alpha \in \{0.6, 0.7\}$ ($\sigma_{\log} \approx 0.2$–$0.35$), partly real and partly a measurement-side artefact: at α=0.7, $p = 113$ the empirical onset lands at 2.16×10^6 parameters — exactly the dim$= 256$ cap of the swept width range — indicating the swept grid is not wide enough to resolve onset at large α. Pooled across all 31 cells, predictiveness is essentially perfect (Spearman $\rho = 0.977$, Kendall

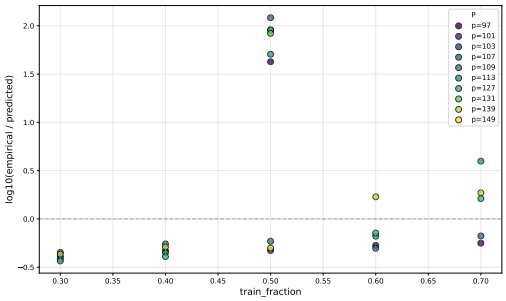
[3] $\alpha = 0.5$ matches the central setting, so the $\alpha = 0.5$ row throughout this section is taken directly from the central sweep (Table 1) rather than re-aggregated by the alpha-sweep pipeline.

Table 7: Learning-rate sweep: within-setting log-residual summary across the 5 primes.

`lr`	n_{primes}	median $\log_{10}(P_{\text{onset}}/\widehat{P}_{\text{cross}})$	std	within-setting verdict
10^{-4}	5	-0.169	0.079	moderate
3×10^{-4}	5	-0.112	0.062	strong
10^{-3}	5	-0.142	0.032	strong
3×10^{-3}	0/5	—	—	no grokking observed in width range
10^{-2}	0/5	—	—	training fails to saturate



(a) Predicted vs. empirical onset, points coloured by `train_fraction`.



(b) Per-cell log-residual against `train_fraction`.

Figure 8: Training-fraction sweep: predicted-vs-empirical scatter and residual trend with the swept axis.

$\tau = 0.890$) and Lin's CCC is high (0.80). The joint $(a, b) = (0, 1)$ calibration test rejects (F=30.0, $p = 10^{-7}$) because the per-cell offset trends systematically with α: from -0.39 dex at $\alpha = 0.3$ to $+0.21$ dex at $\alpha = 0.7$, a $+1.23$ dex per unit α recalibration ($p = 9.4 \times 10^{-6}$). The sceptic-friendly M_3 vs. M_1 comparison is borderline (F=4.45, $p = 0.044$): given $\widehat{P}_{\text{cross}}$, α adds marginal explanatory power, consistent with the smooth α-recalibration captured by the robustness regression. We read this as the same pattern observed for weight decay and depth: within any fixed α the framework's intersection prediction is highly accurate, but the multiplicative offset between $\widehat{P}_{\text{cross}}$ and P_{onset} shifts smoothly across α — a setting-specific recalibration rather than a structural failure.

C.5 Other hyperparameter sweeps

Dropout (matching dropout across capacity, speed, and grokking) and a finer-grained η grid above the current upper bound are scheduled and will be added to this appendix as separate subsections following the *Scope* / figure / pooled / within-setting / verdict template above. Sweeps over architectural axes (depth, attention heads, gated FFN removal, RMSNorm→LayerNorm, RoPE→learned positional embedding, MLP baseline) are reported separately in Section D, where depth is already covered.

D Architectural invariance

Scope and reading guide. The central sweep fixes architecture at depth $L_{\text{depth}} = 2$ with a single attention head ($H = 1$) and gated FFN blocks. To assess whether the speed-intersection prediction is architecture-specific, we re-run the full `capacity` → `speed` → `groks` pipeline at each setting of a swept architectural axis and apply the same two-question evaluation as in Section C: within-setting predictiveness across primes, and cross-setting calibration. Each subsection below uses the same

Table 8: Training-fraction sweep: pooled hypothesis tests on all 31 cells (5 primes $\times$ 4 train-fractions plus the 11-prime α=0.5 central-sweep row). Schema as in Table 1; the robustness row regresses the per-cell log-residual against α.

Sub-claim / Test	Statistic	p-value
(1) Rank predictiveness		
Spearman ρ	0.977	$p_{\text{perm}} < 10^{-4}$
Kendall τ	0.890	2.2×10^{-12}
(2) Calibration to $y = x$		
Lin's CCC (95% CI)	0.804 [0.70, 0.86]	—
Slope $\hat{b}$ (log–log OLS)	1.452	—
Intercept $\hat{a}$	-2.605	—
Joint F-test for $(a = 0, b = 1)$	$F = 29.95$	8.8×10^{-8}
Wilcoxon on log-residuals	median -0.179	4.9×10^{-4}
(3) Sufficiency vs. baselines (nested OLS)		
M_1 vs. M_0 (intersection has signal)	$F = 263.9$	4.4×10^{-16}
M_3 vs. M_2 (intersection adds over hyperparams)	$F = 79.6$	1.1×10^{-9}
M_3 vs. M_1 (hyperparams add over intersection)	$F = 4.45$	0.044
(4) Robustness across the swept axis		
`train_fraction` (numeric)	slope $= +1.23$/unit α	9.4×10^{-6}

Table 9: Training-fraction sweep: within-setting log-residual summary across primes. The α=0.5 row uses the 11-prime / full-seed central-sweep grid; other rows use the 5-prime / 4-seed sub-grid from the alpha sweep.

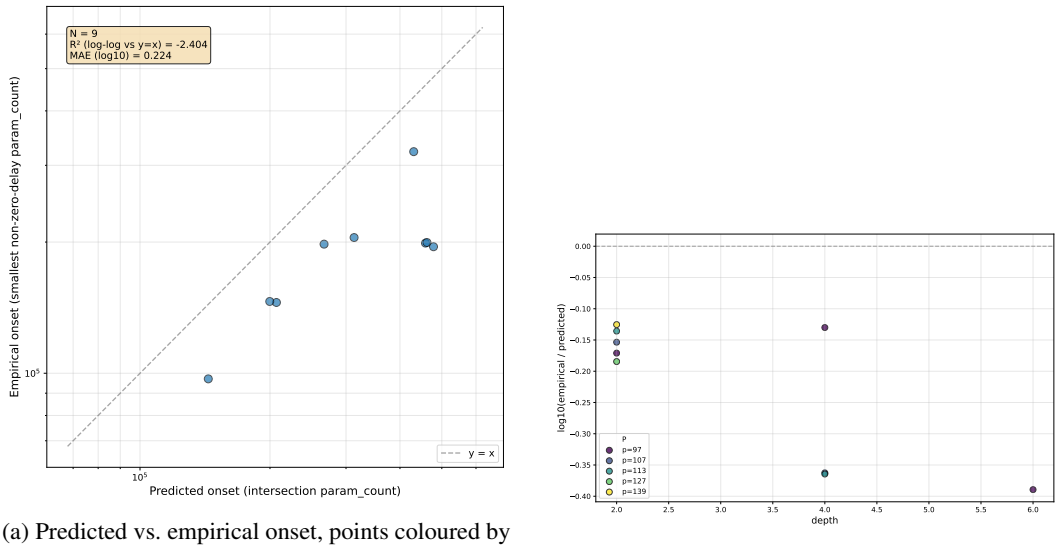
`train_fraction`	n_{primes}	median $\log_{10}(P_{\text{onset}}/\widehat{P}_{\text{cross}})$	std	within-setting verdict
0.3	5	-0.390	0.036	strong
0.4	5	-0.329	0.051	strong
0.5	11	-0.171	0.049	strong
0.6	5	-0.179	0.214	moderate
0.7	5	$+0.211$	0.348	moderate

fixed template (*Scope*, headline figures, pooled tests, within-setting summary, verdict) so that further architectural axes slot in without restructuring.

D.1 Depth scaling

Scope. `depth`$\in \{2, 4, 6, 8, 10\}$ at fixed H=1, matched by parameter count rather than embedding width: target counts $\{5{\times}10^3,\ 10^4,\ 2{\times}10^4,\ 5{\times}10^4,\ 10^5,\ 2{\times}10^5,\ 5{\times}10^5\}$ are realised by selecting, at each depth, the dim closest to each target. Five primes per cell ($p \in \{97, 107, 113, 127, 139\}$); 4 seeds per cell; all other hyperparameters as in Section A.2. `depth`$= 2$ matches the central sweep and serves as an in-sweep baseline. Capacity is re-measured at `depth`$\in \{2, 6, 10\}$ and pinned at $C_{\text{model}} = 2.16$ for missing depths.

Verdict. At the central-sweep architecture (`depth`$= 2$) the predictor reproduces its baseline behaviour: tight per-cell residuals ($\sigma_{\log} = 0.024$) and a consistent constant offset across primes. As depth increases, the diagnostic shifts in two ways. First, the constant offset becomes more negative — empirical onset arrives earlier (relative to the predicted $\widehat{P}_{\text{cross}}$) at deeper models — and the across-axis robustness regression captures this trend at -0.061 dex per unit depth (p=0.012). Second, and more interpretively important, deeper models ($L_{\text{depth}} \geq 6$) routinely fail to exhibit a speed crossover within the param-count range we sweep ($\leq 5{\times}10^5$): $T_{\text{mem}}(P)$ stays above $T_{\text{gen}}(P)$ throughout, so $\widehat{P}_{\text{cross}}$ is undefined while empirical onsets still occur. The pooled $\rho = 0.60$ and the marginal M_3 vs. M_1 test (p=0.095, only weakly rejecting the additional explanatory value of depth) reflect both the small valid-cell count and the depth-dependent recalibration. We read this as the framework remaining well-defined within each fixed depth, but with the speed-curve geometry — and hence the calibration constant — shifting with architecture, consistent with depth changing how memorisation



(a) Predicted vs. empirical onset, points coloured by `depth`.

(b) Per-cell log-residual against `depth`.

Figure 9: Depth-scaling sweep: predicted-vs-empirical scatter and residual trend with the swept axis.

Table 10: Depth-scaling sweep: pooled hypothesis tests on the 9 valid cells (out of 25; 16 cells at `depth`≥ 4 have no recorded intersection within the swept param-count range, see text). Schema as in Table 1; the robustness row regresses the per-cell log-residual against L_{depth}.

Sub-claim / Test	Statistic	p-value
(1) Rank predictiveness		
Spearman ρ	0.600	$p_{\text{perm}} = 0.10$
Kendall τ	0.444	0.119
(2) Calibration to $y = x$		
Lin's CCC (95% CI)	0.392 [0.07, 0.64]	—
Slope $\hat{b}$ (log–log OLS)	0.603	—
Intercept $\hat{a}$	1.955	—
Joint F-test for $(a = 0, b = 1)$	$F = 31.6$	3.1×10^{-4}
Wilcoxon on log-residuals	median -0.171	3.9×10^{-3}
(3) Sufficiency vs. baselines (nested OLS)		
M_1 vs. M_0 (intersection has signal)	$F = 13.7$	7.7×10^{-3}
M_3 vs. M_2 (intersection adds over hyperparams)	$F = 21.8$	3.4×10^{-3}
M_3 vs. M_1 (hyperparams add over intersection)	$F = 3.93$	0.095
(4) Robustness across the swept axis		
depth (numeric)	slope $= -0.061$/unit L_{depth}	0.012

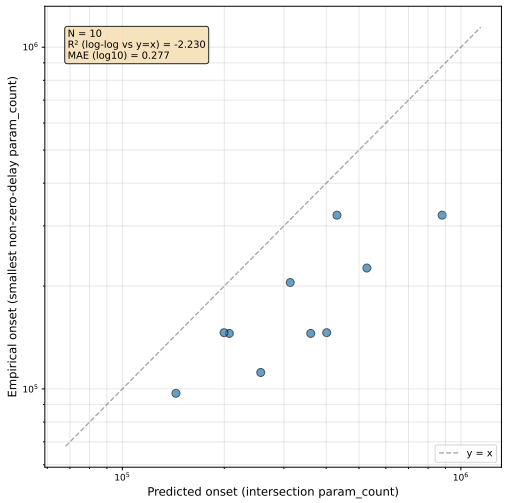
and generalisation each scale with parameter count rather than just where they cross. Extending the param-count range (or, equivalently, the dim grid) to recover well-defined intersections at $L_{\text{depth}} \geq 6$ is left for future work.

D.2 Other architectural sweeps

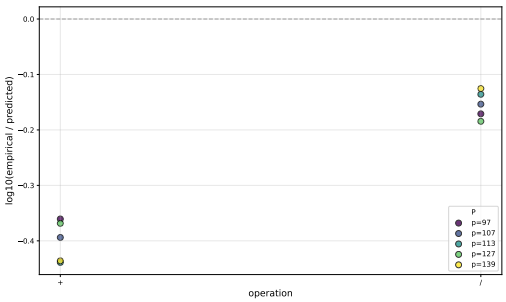
A number-of-heads sweep ($H \in \{1, 2, 4, 8\}$ at fixed depth) and architectural-variant sweeps (gated FFN removal, RMSNorm→LayerNorm, RoPE→learned positional embedding, MLP baseline) are scheduled and will be added as further subsections following the same template.

Table 11: Depth-scaling sweep: within-setting log-residual summary. At `depth`≥ 4 only a subset of primes yields a measured intersection within the swept param-count range; the remaining cells have $T_{\text{mem}}(P) > T_{\text{gen}}(P)$ throughout the explored range, so $\widehat{P}_{\text{cross}}$ is undefined while empirical onsets are still recorded.

`depth`	n_{primes}	median $\log_{10}(P_{\text{onset}}/\widehat{P}_{\text{cross}})$	std	within-setting verdict
2	5	-0.154	0.024	strong
4	3/5	-0.363	0.135	weak (small N, large spread)
6	1/5	-0.389	—	under-resolved
8	0/5	—	—	no intersection in range
10	0/5	—	—	no intersection in range



(a) Predicted vs. empirical onset, points coloured by operation.



(b) Per-cell log-residual against operation.

Figure 10: Task-addition sweep: predicted-vs-empirical scatter and residual trend with the swept axis.

E Task invariance

Scope and reading guide. The central sweep uses modular division. To assess whether the speed-intersection prediction extends to other modular operations, we re-run the full pipeline for each operation and apply the same two-question evaluation as in Section C: within-task predictiveness across primes, and cross-task calibration of the predictor. Each subsection below uses the same fixed template (*Scope*, headline figures, pooled tests, within-setting summary, verdict) so that further task families slot in without restructuring.

E.1 Modular addition

Scope. Operation $\circ \in \{+, /\}$ at the same five primes ($p \in \{97, 107, 113, 127, 139\}$); architecture, optimiser, and aggregation as Section A.2. For $\circ = +$, the dataset enumerates all p^2 pairs (rather than $p(p-1)$ for $/$), so $K_{\text{mem}}(p, \alpha)$ and $n_{\text{equiv}}(p, \alpha)$ are recomputed accordingly. The $\circ = /$ cells reuse the central-sweep speed and grokking runs and serve as an in-sweep baseline.

Verdict. Within each operation, log-residuals are tight ($\sigma_{\log} \leq 0.04$, Table 13): the predictor ranks the five primes correctly and incurs only a constant multiplicative offset within each task (the $\circ = /$ row reproduces the central-sweep result at the same five primes). Across operations, the predictor over-shoots empirical onset by $\approx 2.5\times$ for $+$ versus $\approx 1.4\times$ for $/$, a gap that the operation indicator captures cleanly: the categorical robustness test is significant ($F = 155$, $p = 10^{-6}$) and the sufficiency comparisons rank $M_3 > M_1$ and $M_3 > M_2$. We interpret this as expected task-

Table 12: Task-addition sweep: pooled hypothesis tests on the 10 cells (5 primes $\times$ 2 operations). Schema as in Table 1; the robustness row treats operation as a categorical factor.

Sub-claim / Test	Statistic	p-value
(1) Rank predictiveness		
Spearman ρ	0.801	$p_{\text{perm}} = 7.5 \times 10^{-3}$
Kendall τ	0.644	0.011
(2) Calibration to $y = x$		
Lin's CCC (95% CI)	0.395 [0.12, 0.58]	—
Slope $\hat{b}$ (log–log OLS)	0.634	—
Intercept $\hat{a}$	1.740	—
Joint F-test for $(a = 0, b = 1)$	$F = 35.0$	1.1×10^{-4}
Wilcoxon on log-residuals	median -0.273	2.0×10^{-3}
(3) Sufficiency vs. baselines (nested OLS)		
M_1 vs. M_0 (intersection has signal)	$F = 16.1$	3.9×10^{-3}
M_3 vs. M_2 (intersection adds over hyperparams)	$F = 263$	8.3×10^{-7}
M_3 vs. M_1 (hyperparams add over intersection)	$F = 82.8$	4.0×10^{-5}
(4) Robustness across the swept axis		
operation (categorical)	$F = 155$	1.6×10^{-6}

Table 13: Task-addition sweep: within-setting log-residual summary across the 5 primes.

Operation	n_{primes}	median $\log_{10}(P_{\text{onset}}/\widehat{P}_{\text{cross}})$	std	within-setting verdict
$+$	5	-0.394	0.037	strong
$/$	5	-0.154	0.024	strong

specific calibration — $T_{\text{mem}}(P)$ on random labels of equivalent complexity is operation-agnostic by construction, but $T_{\text{gen}}(P)$ for $+$ is consistently faster than for $/$, shifting the intersection by a constant in log space — and not a within-task failure of the framework.

E.2 Other task sweeps

Modular multiplication and modular subtraction are scheduled and will be added as further subsections following the same template; permutation composition (e.g. S_5) is a longer-term target requiring new task plumbing.